Journal of The Electrochemical Society, **163** (10) A2464-A2474 (2016)
0013-4651/2016/163(10)/A2464/11/$33.00 © The Electrochemical Society

In Situ Formed Layered-Layered Metal Oxide as Bifunctional Catalyst for Li-Air Batteries

Mehmet Nurullah Ates,[a,c] Iromie Gunasekara,[a] Sanjeev Mukerjee,[a,*] Edward J. Plichta,[b] Mary A. Hendrickson,[b] and K. M. Abraham[a,,z]**

[a]*Northeastern University Center for Renewable Energy Technology, Department of Chemistry and Chemical Biology, Northeastern University, Boston, Massachusetts 02115, USA*
[b]*Power Division, US Army RDECOM CERDEC CP&I, RDER-CCP, Aberdeen Proving Ground, Maryland 21005, USA*

The electrochemical activity of a Li-air battery cathode catalyst derived from the lithium rich layered-layered metal oxide of the formula $0.5Li_2MnO_3.0.5LiMn_{0.5}Ni_{0.35}Co_{0.15}O_2$ is reported. The catalyst formed in-situ by electrochemically de-lithiating this metal oxide embedded in a high surface area carbon matrix behaved as a bifunctional catalyst for O_2 reduction reaction (ORR) and O_2 evolution reaction (OER) in a non-aqueous Li-O_2 cell. Cyclic voltammetry (CV) in both half and full cells revealed enhanced OER and ORR catalytic activity by: i-) displaying a more positive potential shift during ORR, ii-) stabilizing the initial ORR product LiO_2, and iii-) showing an additional potential step in the oxidation of the ORR products. In the CV of catalyzed cells, a reduction peak appeared before the main peroxide (O_2^{2-}) formation peak suggesting that the catalyst stabilizes the superoxide (O_2^-) formed prior to the formation of peroxide. Evidence for LiO_2 as the initial discharge product was obtained from both the Raman spectrum and X-ray diffraction (XRD) pattern of Li-air cell cathodes after galvanostatic discharge to 2 V. Surface features for the discharged cathodes obtained from Field Emission Scanning Electron Microscope (FESEM) unveiled dissimilar morphologies for the discharge products from catalyzed and uncatalyzed cells, originating from different nucleation mechanisms. The catalyzed cells exhibited longer cycle life than uncatalyzed cells under similar cycling conditions.
 [DOI: 10.1149/2.0111613jes]

Manuscript submitted June 29, 2016; revised manuscript received September 1, 2016. Published September 9, 2016.

Conventional lithium ion batteries with one-electron reversible transfer per metal in transition metal oxide cathodes are not capable of a 300-mile (500 km) driving range for all-electric vehicles on a single charge. Advanced batteries having at least 50 percent higher energy density than today's best Li-ion battery are needed to realize such electric vehicles. In order to overcome the constraints imposed on the reversible capacity of cathode materials by the lithium intercalation reaction, it is increasingly becoming necessary to change the electrode reaction process to one of atom displacement reaction involving multiple electron transfer per atom. In this connection rechargeable non-aqueous lithium-air (i.e. Li/O_2) batteries[1,2] have opened up new horizons to search for higher energy density batteries that could achieve the 300-mile EV driving range. Now there is consensus that the ORR mechanism in non-aqueous electrolytes is different from that observed in aqueous electrolytes relevant to H_2/O_2 fuel cells. Generally O_2 reduction reactions (ORR) in non-aqueous electrolytes, including organic electrolytes and room temperature ionic liquids, occur in the following steps:[3–6]

Step 1: $O_2 + Li^+ + e^- \rightarrow LiO_2$ (initial one-electron electrochemical reduction step which can rarely be observed)

Step 2: $2LiO_2 \rightarrow Li_2O_2 + O_2$ (chemical decomposition to the common discharge product)

Step 3: $LiO_2 + e^- + Li^+ \rightarrow Li_2O_2$ (electrochemical reduction of initial reduction product LiO_2 to the common discharge product)

Step 4: $Li_2O_2 + 2e^- + 2Li^+ \rightarrow 2Li_2O$ (electrochemical reduction product at low potentials possible in a potentiodynamic experiment)

The oxygen evolution reaction (OER) paths do not necessarily follow the reverse of those in the ORR. The most probable OER reactions are:

Step 5: $LiO_2 \rightarrow O_2 + Li^+ + e^-$

Step 6: $Li_2O_2 \rightarrow O_2 + 2Li^+ + 2e^-$

Step 7: $Li_2O \rightarrow 1/2O_2 + 2Li^+ + 2e^-$

The LiO_2 formed in step 1 is very short-lived in most non-aqueous electrolytes due to the moderately soft basicity of O_2^- which discourages its association with the hard Lewis acid Li^+. The superoxide specie in most cases decomposes readily to peroxide (O_2^{2-}) (step 2) which is a hard base and it readily combines with Li^+ to form Li_2O_2. In high donor number (DN) electrolytes such as dimethyl sulfoxide (DMSO, DN = 29.8), the acidity of Li^+ ions in solution is substantially decreased by its solvation with DMSO such that $(DMSO)_nLi^+$ acts as a soft acid which enables the superoxide species to become ion-paired with Li^+ in DMSO. In such cases, the $(DMSO)_nLiO_2$ has a relatively longer lifetime in solution. Throughout this work, we used tetra ethylene glycol dimethyl ether (TEGDME) based electrolytes which has a low Gutmann DN (DN = 16.6) providing short life time for the superoxide initially formed in the reduction of O_2. As a result the superoxide quickly decomposes according to the reaction in step 2 in this electrolyte. The discharge product of an uncatalyzed Li-O_2 cell utilizing TEGDME/LiX where X^- is $CF_3SO_3^-$ or PF_6^- is Li_2O_2.[5]

Several technical issues and possible solutions pertaining to the Li air batteries have been documented.[3,7–10] Among them, appropriate cathode catalysts[11–13] to enhance the ORR and OER kinetics and reversibility is well recognized. In this paper we show that i-) the layered-layered metal oxide of the approximate composition $0.5MnO_2.Mn_{0.5}Ni_{0.35}Co_{0.15}O_2$ obtained by the electrochemical delithiation of $0.5Li_2MnO_3.0.5LiMn_{0.5}Ni_{0.35}Co_{0.15}O_2$ promotes the stabilization of the initial ORR product LiO_2 by the catalyst which in turn lowers the voltage polarization of the oxidation reaction during Li-O_2 cell charging and ii-) the stabilization of the initial ORR product LiO_2 by the catalyst also lowers the activation energy of oxygen reduction reaction (Li-O_2 cell discharge) which improves the power density of the battery.

Experimental

Chemical reagents.—Anhydrous grade ≥99.8% acetonitrile (CH_3CN), purum grade ≥98.0% tetraethylene glycol dimethyl ether (TEGDME), anhydrous grade ≥99.5% 1,2- dimethoxyethane (DME), and electrochemical grade tetrabutylammonium hexafluorophosphate ($TBAPF_6$) were purchased from SigmaAldrich, Allentown, PA. Purolyte lithium hexafluorophosphate ($LiPF_6$) certified to contain less than 20.0 ppm water was purchased from Novolyte Technologies and used without further treatment. Metals basis 99.9% Li foil purchased from Alfa Aesar Company was used as anode of the Li-O_2 cells. Soon after their arrival, all these reagents were stored in an MBraun Labmaster 130 argon-filled glove box with moisture maintained below 5 ppm.

Synthesis of the catalyst ($0.5Li_2MnO_3.0.5LiMn_{0.5}Ni_{0.35}Co_{0.15}O_2$).—In a synthesis, appropriate amounts of $Mn(Ac)_2.4H_2O$ (Sigma Aldrich >99%), $Ni(NO_3)_2.6H_2O$ (Alfa Aesar-Puratronic)

*Electrochemical Society Member.
**Electrochemical Society Fellow.
[c]Present address: Xerion Advanced Battery Corp., Champaign, Illinois 61820, USA.
[z]E-mail: kmabraham@comcast.net

and $Co(NO_3)_2.6H_2O$ (Alfa Aesar- Puratronic) taken in the proper molar ratio were thoroughly dissolved in distilled water in a Teflon beaker at room temperature to prepare ultimately a catalyst precursor material of the composition $0.5Li_2MnO_3.0.5LiMn_{0.50}Ni_{0.35}Co_{0.15}O_2$. Nitric acid and glycine (Sigma Aldrich >99%) were added to the aqueous solution containing the metal cations before heating the solution on a hot plate. The temperature of the hot plate reached around 120 °C when the nitric acid and glycine mixture initiated a combustion reaction of the metal salts. Different amounts of glycine, a source of fuel, were used to optimize and control the combustion reaction which takes place after an hour. Glycine is known to be a complexing agent for transition metal ions due to the presence of both carboxylic acid and amino groups in its structure. The metal acetate precursor used in the reaction produces a large amount of gas by-product, whose evolution leads to open porous microstructures in the combustion reaction product. The Li precursor, $LiOH.H_2O$ (Alfa Aesar >99.995%), was added in stoichiometric quantity to the combustion product and the mixture was fired at 480 °C for 3 h and then re-grounded and pelletized and fired at 900 °C for 3 h under air atmosphere.

Potential sweep rate studies.—A three electrode system was employed to assess the initial OER and ORR in an air-tight cell along with a gas-inlet constructed from a polypropylene jar and lid which kept the cell electrodes separated and intact. All electrochemical measurements were carried out in a glove box with moisture level kept under 5 ppm. An Autolab potentiostat (PGSTAT-30) was used for electrochemical measurements. The counter electrode was a piece of Pt gauze which was hung from the cell lid to the electrolyte. The air-tight cell contained approximately 20 ml of the electrolyte comprised of 0.1 M $LiPF_6$ dissolved in CH_3CN. The reference electrode Ag/Ag^+ was prepared with a silver wire immersed into 100 mM $TBAPF_6$, 10 mM $AgNO_3/CH_3CN$ solution in a borosilicate glass sleeve. The sleeve was separated from the electrolyte by a Vycor frit to prevent the solution from the reference electrode leaking into the electrolyte. A 5 mm diameter glassy carbon (GC) disk was used as the working electrode. It was covered with a thin layer of carbon black prepared from an ink containing the high surface area carbon Ketjen Black-300 (90 wt%-KB300-weight-percent) and polyvinylidene fluoride (PVDF-10 wt%) dissolved in N-methyl-2-pyrrolidone (NMP) solvent. Thin carbon films formed on the GC carbon surface was kept always the same (i.e. 100 $\mu g/cm^2$) using microliter ink aliquots. The catalyst loaded GC electrode was prepared using the same protocol except that the ink was composed of 80 wt% KB300, 10 wt% lithium metal oxide catalyst and 10 wt% PVDF. Before each experiment the GC disk electrode was polished with 0.05 mm alumina paste followed by a thorough rinsing with deionized water. The GC electrodes were dried overnight under vacuum at 100 °C before transferring them to the glove box. The potential scale of the half-cell measurements were converted into Li scale as described previously (0 V vs Ag/Ag^+ equals to 3.5 V vs Li/Li^+).[14] High purity oxygen gas was purged into the electrolyte for 30 minutes before running the CV tests and once the electrolyte was saturated the O_2 flow was stopped. The electrolyte evaporation was negligible during oxygen gas purging.

Li-O_2 cell studies.—Li-O_2 cell cathodes were fabricated with a loading of at least 2–3 mg/cm^2 carbon for each cell. The Li-O_2 cells were constructed as we previously described.[5] The catalyzed cathode was prepared from a mixture of 80 wt% of the KB300, 10 wt% of the catalyst and 10 wt% polyvinylidene fluoride (PVDF-Kynar 2801) as binder. The cathode mixture was dissolved in N-methyl 2-pyrrolidone (NMP, Sigma Aldrich >99%) and the resulting slurry was cast onto a carbon cloth. The wet carbon cloth was then transferred to a vacuum oven for drying purpose. The uncatalyzed cathode was prepared using the same protocols without catalyst addition. Li-O_2 cells were built with ribbons of this cathode and Li foil anode (33 mm diameter and 1.5 mm thick), separated by a porous propylene membrane separator, and filled with 1 M $LiPF_6$/TEGDME electrolyte. All assembly procedures were performed in an MBraun Labmaster 130 glove box where the water level was kept under 5 ppm. The assembled cells were sealed in aluminized bags and transferred to another glove box where they were placed in cell containers built for cell cycling experiments with a constant oxygen flow. Unless mentioned otherwise, the cells were cycled between 2 and 4.6 V at room temperature on an Arbin Instrument BTZ2000 model cycler. The cell was discharged at a depth of 400 mAh/g at 0.1 mA/cm^2. Electrochemical Impedance Spectroscopy (EIS) measurements were performed over an AC frequency range of 100 kHz to 10 mHz with a 5 mV amplitude AC sine wave on a Voltalab PGZ402 model potentiostat in order to evaluate and compare the impedance responses of the cells. The Voltalab potentiostat was also used for slow sweep cyclic voltammetry (CV) experiments ranging from 25 to 100 μV/s sweep rates.

Characterization of the catalyst and the discharge product from Li-O_2 cells.—The pristine catalyst precursor, $0.5Li_2MnO_3.0.5LiMn_{0.5}Ni_{0.35}Co_{0.15}O_2$, was characterized by XRD, FESEM, high resolution transmission electron microscope (HRTEM), selected area diffraction (SAED) and Raman spectroscopic techniques in detail. X-Ray Diffraction patterns of the catalyst and discharged samples were obtained using a Rigaku Ultima IV diffractometer with CuKα radiation. For ex-situ XRD experiments, harvested electrodes from cycled Li-O_2 cells were removed and cut to fit the XRD quartz sample holder, then sealed with Kapton polyimide tape thoroughly before recording the X-ray scans. Morphological and structural investigations were performed with a Hitachi S-4800 FESEM. For FESEM investigation discharged cathodes were rinsed with anhydrous dimethyl carbonate (DMC) to remove possible electrolyte residue before examination. Later, the discharged samples were mounted on carbon adhesives which were affixed to FESEM sample holder. The holder then was put into the antechamber of glove box and left under dynamic vacuum for overnight. The transfer time of the discharged samples from the glove box antechamber to FESEM sample holder rod was less than a minute. A JEOL 2010F model HRTEM was utilized for structural investigations of the pristine catalyst. The samples for HRTEM were prepared by dispersing powders into an ethanol solution followed by a few minutes of sonication, and then one or two drops of the dispersed solution was dropped onto Cu holey grid. Raman spectra was collected with a confocal Raman microscope using a solid state 488 nm excitation laser with a power of 23 mW and 600 grooves/mm grating. The calibration of the instrument was done with a Si chip which gives a strong peak at 520 cm^{-1}. The objective lens for the measurement was 100 X.

XAS measurements were performed at beam lines X-3A and X-18A of the National Synchrotron Light Source at Brookhaven National Laboratory located in Upton, New York on Long Island. The data were processed using the Athena software program. Scans were calibrated, aligned and normalized. Experimental details can be found in our previous publication.[15] XAS data was obtained from Li-ion cells which allowed us to trace the expected intercalation phenomena in Li-O_2 cells. Since the loading of the catalyst in Li-O_2 cells were very small, we employed Li-ion cells in the beamlines to obtain the X-ray absorption data presented in this paper. The redox behavior of the catalyst collected from the Li-ion test cells shed light on its valence state changes during the charge and discharge of Li-O_2 cells.

Results and Discussion

We have studied the usefulness of the previously synthesized and characterized Li-rich layered-layered metal oxide cathode material for Li-ion batteries of the formula $0.5Li_2MnO_3.0.5LiMn_{0.5}Ni_{0.35}Co_{0.15}O_2$. We prepared this cathode as catalyst precursor for Li/O_2 batteries using a morphology driven synthesis method.[15] The active catalyst is synthesized in-situ in the Li/O_2 cell by charging it first to about 4.6 V before admitting O_2 into the cell. Extraction of Li from or its insertion into the layered-layered composite oxide structure does not affect the overall crystal structure of the material except that small lattice

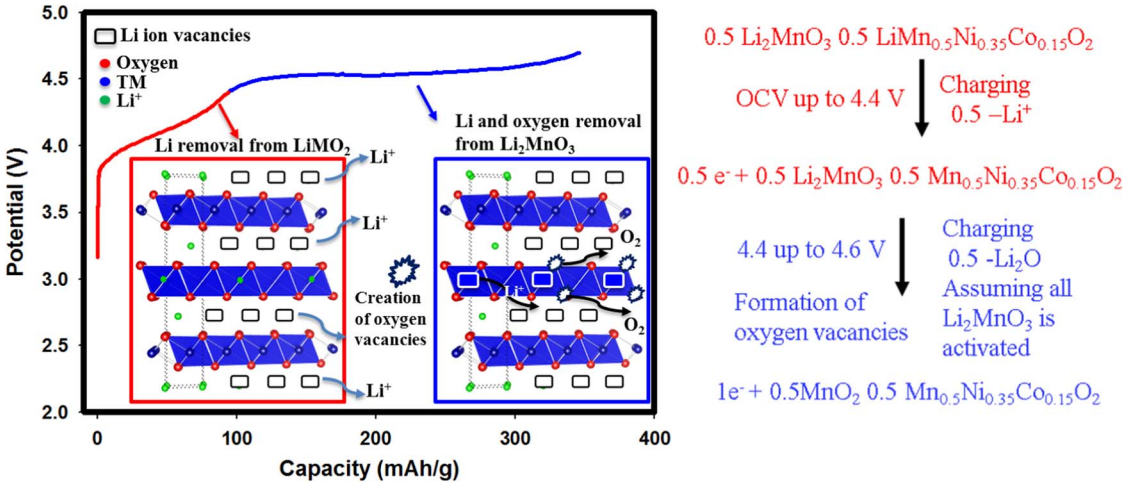

Figure 1. Electrochemical activation and creation of the oxygen vacancies in the catalyst in Li-ion cell along with the structural visualizations for each step and their corresponding reaction pathways depicted on the right side of the figure. The electrolyte employed in this cell was 1 M $LiPF_6$ dissolved in EC:DMC.

parameter changes occur. Overall, the structure remain intact during the topotactic reaction of Li^+ accompanying the potential changes in the Li cell. During charging and discharging of the Li-O_2 cell, the small amount of insertion and extraction of Li^+ occurring in the catalyst tune the valence state (i.e. d orbital emptying/filling) of each transition metal such that the lithium rich metal oxide plays a unique role as a bifunctional catalyst. The other motivation of our work on this catalyst has been that while charging it up to 4.6 V, irreversible Li_2O removal from the parent oxide structure creates oxygen vacancies in the metal oxide lattice, a promising strategy for tailoring the O_2 binding efficacy to the catalytic sites during O_2 reduction reaction. Intentionally formed surface defects have spurred great interest among energy conversion and storage researchers.[16–18]

Characterization of the active catalyst.—Electrochemical activation of the catalyst precursor and the formation of oxygen vacancies in the metal oxide catalyst framework $0.5MnO_2.Mn_{0.5}Ni_{0.35}Co_{0.15}O_2$ are depicted in Figure 1. The Li removal from the two segments of the layered-layered metal oxide $0.5Li_2MnO_3.0.5LiMn_{0.5}Ni_{0.35}Co_{0.15}O_2$ produces the layered composite metal oxide consisting of two layered metal oxide segments that are structurally integrated through matching lattices and are electrochemically compatible at high potentials i.e. 4.6 V. After the irreversible Li_2O removal at this high potential,[19–22] a regular $LiMO_2$ single layered structure is formed during discharge. In the catalyzed Li-O_2 cells, during the course of cycling one can readily see that similar reaction takes place in the catalyst even if the amount of catalyst is very small in the oxygen cell cathode. The reaction steps during the initial activation step of the catalyst are schematized on the right side of the Figure 1. Initially Li is removed from the $LiMn_{0.5}Ni_{0.35}Co_{0.15}O_2$ segment of the composite oxide. Oxygen vacancies are formed during the activation of Li_2MnO_3 at the second step between 4.4 and 4.6V. If the cell is exposed to O_2 gas flow, we believe these sites facilitate the O_2 adsorption during ORR in non-aqueous media as reported earlier for a pyrochlore catalyst.[16]

The formation of oxygen vacancies is crucial since vacant oxygen sites are favorable for the initial adsorption of O_2 molecules and facilitate the first reduction of O_2 to superoxide instead of peroxide ions. Cheng et al. studied the improved ORR behavior of MnO_{2-x} ($x = 0.02–0.08$) with oxygen vacancies by means of electrochemical behavior and density functional theory (DFT).[17] They found that vacant oxygen sites in MnO_{2-x} enabled catalytic sites to bind oxygen molecules stronger than that of MnO_2 without surface defect during ORR.

As demonstrated in Figure 2a, the XRD patterns of the pristine catalyst precursor features two space groups that are structurally integrated to each other as phases C2/m and R3-m, both have the same lattice plane diffraction lines with the exception of those located between 21–27 2θ degrees. These reflections can only be assigned to C2/m space group as shown at the bottom of Figure 2a. The rest of the peaks can therefore be considered the combination of the two phases. The detailed XRD refinement results in addition to electrochemical performance of this catalyst in Li-ion cells was published recently.[15] We found no capacity fade in Li-ion cells with this cathode at high and low rates. Figure 2b displays the Raman spectra collected for the catalyst precursor. The spectra clearly exhibits three major reflections. The strongest peak at 598 cm^{-1} and the peak located at 474 cm^{-1} is due to the out of plane M-O stretching and in plane O-M-O bending from $LiMO_2$ with R3m space group, respectively. The Mn-O stretching from Li_2MnO_3 with C2/m space group can be seen at 423 cm^{-1}.[23,24] XRD data together with Raman spectrum supports the view that the composite oxide structure has two phases at the bulk level.

Although XRD and Raman data provided an average structural feature for the catalyst, in order to get insight into the composite nature of the catalyst at the atomic level, we have employed HRTEM and SAED techniques to unravel the existence of Li_2MnO_3 with C2/m space group. Figure 2c shows the image for KB300 carbon obtained from HRTEM showing the nanosize carbon particles. The inset in this figure displays the Fourier Transformed (FT) feature of the image in Figure 2c suggesting the amorphous nature of the carbon which is expected. Figure 2d also shows the bright field HRTEM image of the catalyst along with the SAED patterns revealing the polycrystalline nature of the composite oxide at the nano scale level. Each ring can easily be assigned to the planes that appearing in the XRD patterns presented in Figure 2a. As can be observed from Figure 2e, the calculated d spacing between lattice fringes was around 4.7 Å and perfectly matched with the XRD value (corresponding to the first peak in the XRD pattern). The inset of Figure 2e displays an average particle size, i.e. 200–250 nm, for the catalyst. Additional information on the HRTEM and SAED analysis for the pristine catalyst can be found in our previous paper.[15]

Electrochemistry of the O_2 electrode.—*Fast sweep cyclic voltammetry studies:*.—Figure 3 depicts the CV results for O_2 electrochemistry on plain glassy carbon (GC), KB300 cast on GC (KB300/GC) and catalyst embedded onto KB300 cast on GC (catalyst+ KB300/GC) electrodes. They were run both in the presence of oxygen and its absence (argon purged) at a scan rate of 10 mV/s in 0.1 M $LiPF_6$ dissolved in CH_3CN. Acetonitrile medium was selected since it has high ionic conductivity, oxygen solubility and wide electrochemical window which allowed us to run the CV studies at high potentials without

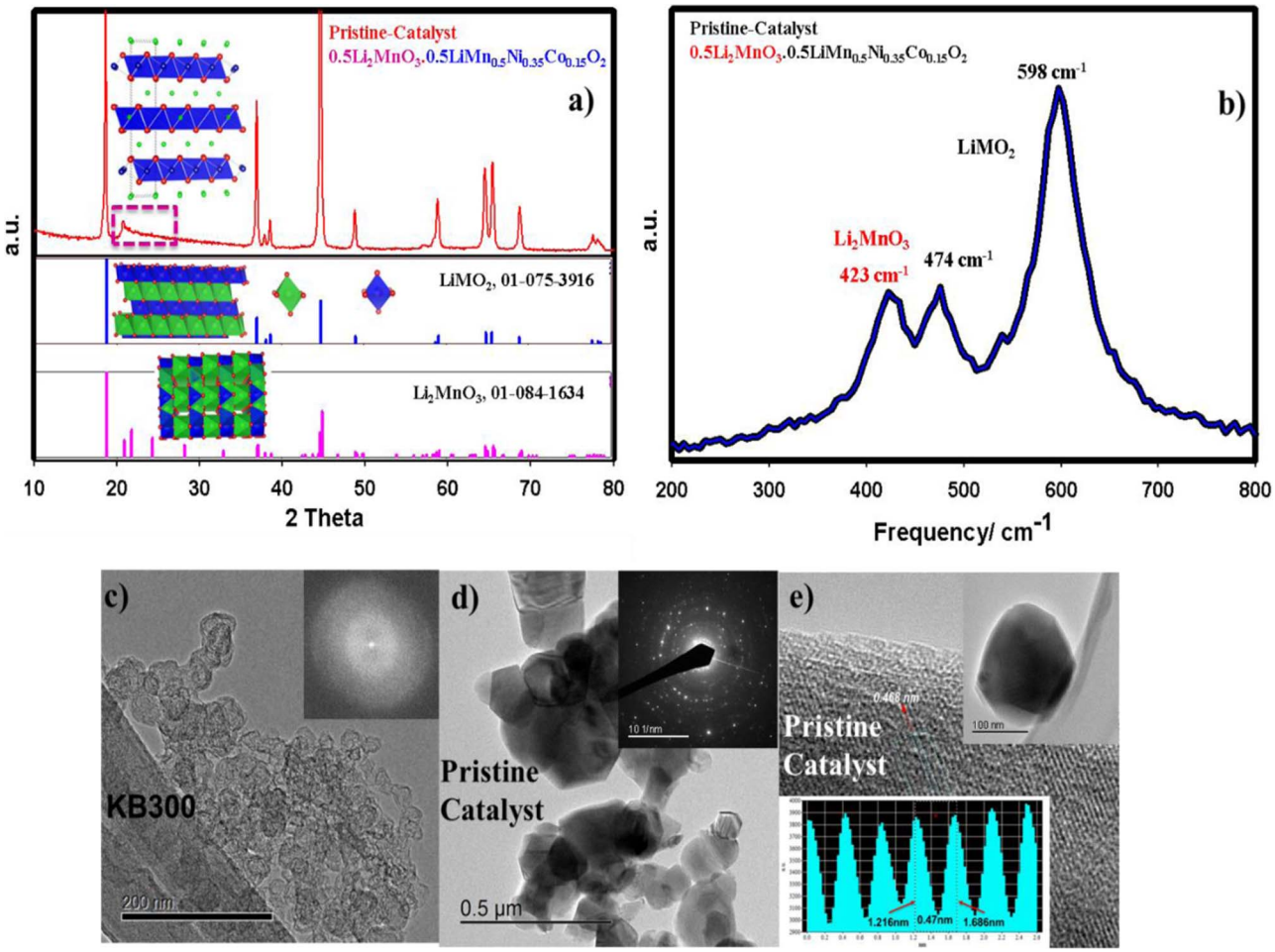

Figure 2. a) XRD patterns of the pristine (catalyst) lithium rich metal oxide along with crystal structures. Green balls and polyhedrons indicate Li ions and Li-O environment, respectively. Blue polyhedrons indicate M-O environment and red balls represent oxygen atoms. b-) Raman spectra of the pristine catalyst precursor. c-) HRTEM image of KB300 carbon particles and FT image of it indicating amorphous feature. d-) HRTEM figure of catalyst and its SAED ring pattern indicating polycrystalline nature of the catalyst. e-) calculated d-spacing between lattice fringes of as-synthesized catalyst precursor.

decomposing the electrolyte. The stability of the electrolyte was confirmed by a CV scan of the catalyst embedded KB300/GC electrode under argon purge which did not show any appreciable current even at 4.7 V. This is shown with purple color in Figure 3. The same experiment also demonstrated that there is no electroactive species both in the electrolyte and catalyst itself. As displayed with blue color in Figure 3, CV on plain GC gives rise to an O_2 reduction peak around 2.5 V which is in a good agreement with previous observations.[14]

Because plain GC does not have porosity or catalytic active sites for ORR, the current is small and as a result the scale was drawn on the right side of the plot for lucid comparison. Although there is a sharp peak for ORR, no appreciable OER peak was observed on plain GC carbon. This can be attributed to the passivation of the electrode surface by the ORR product, Li_2O_2. The catalyst-free high surface area KB300 deposited on GC (KB300 /GC), which is shown in black color, exhibited higher currents both during ORR and OER due to its high surface area. The remarkably enhanced OER and ORR activities of the catalyzed GC (catalyst/KB300/GC) electrode coded in red color in Figure 3. The specific regions corresponding to OER and ORR activities are magnified and plotted on the right hand side of Figure 3. During the initial oxygen reduction (ORR), the improved voltage response is evidenced by a positive voltage shift of ∼150 mV. Surprisingly, the reverse process (OER) also suggests a different oxidation mechanism for the catalyzed cell compared to the uncatalyzed cell. During OER, a new peak appeared at around 3.5 V in the catalyzed cell, that is absent in the uncatalyzed cell. This indicates the oxidation of a stabilized discharge product formed on the catalyst during the ORR process. This process will be discussed later. The higher current densities both during ORR and OER together with improved potential responses lead us to conclude that the very thin film of lithium-rich metal oxide deposited on the GC catalyzes both ORR and OER processes. One should keep in mind that the surface area of catalyst (∼3.5 m^2/g based on BET measurements) is significantly lower than that of high surface KB300 (∼760 m^2/g). This piece of information advocates that the enhanced OER and ORR performances of the catalyzed cell is not due to surface area but rather to the intrinsic property of the catalyst arising from the d orbitals of the transition metals in the catalyst which promotes ORR and OER processes (vide infra).

Li-O_2 full cells.—Although the results presented in Figure 3 are intriguing, the solvent selected in the half-cell studies are not practical due to instability of Li foil in the presence of CH_3CN. We, therefore, conducted the CV studies in a similar fashion described above in full-cells in which Li foil was employed as an anode in combination with an electrolyte composed of 1 M $LiPF_6$ dissolved in TEGDME. The detailed full-cell CV data are depicted in Figure 4a–4d. We first ran the CV scans in the potential range of 2.5–4.3 V in order to discern the initial ORR product and its characteristic OER path. Figure 4a displays several CV scans and each of them coded with different colors.

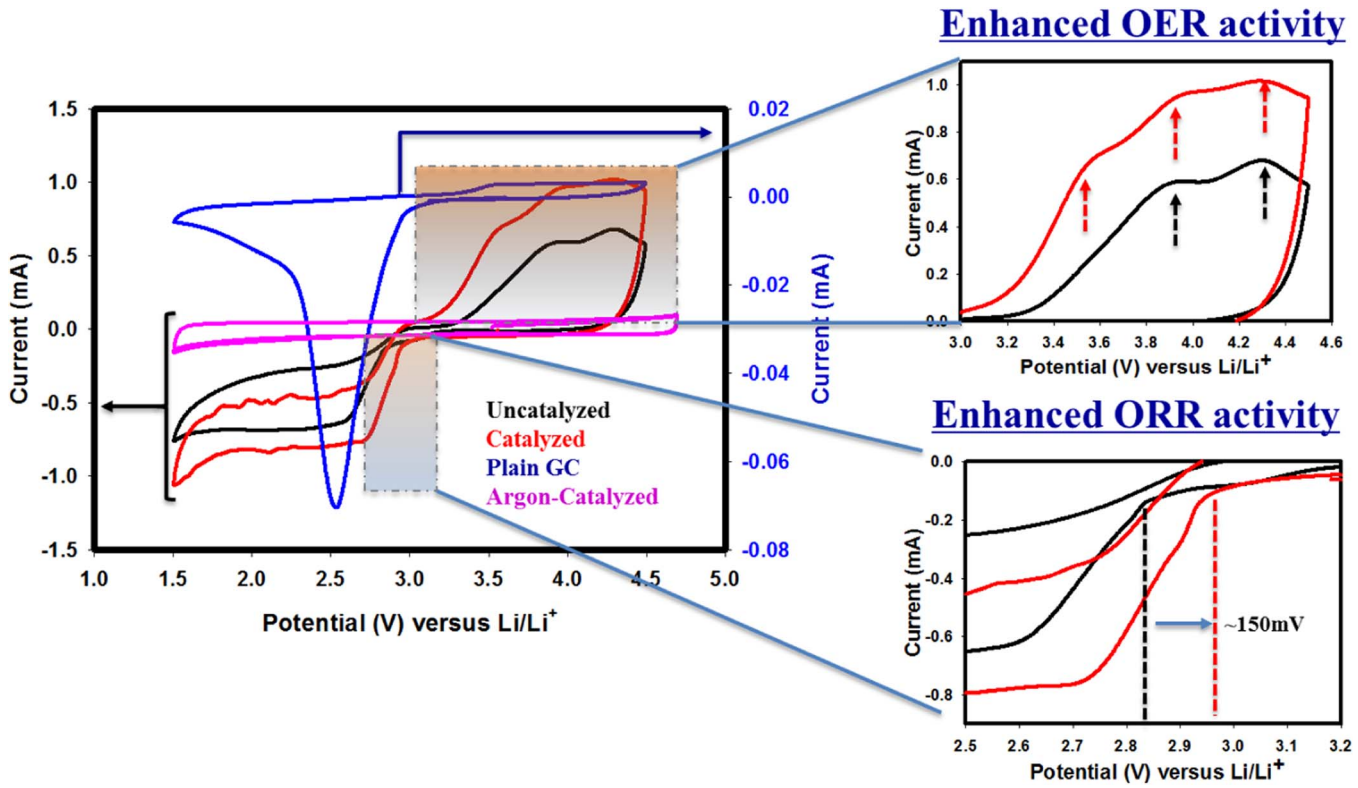

Figure 3. Cyclic voltammograms of plain glassy carbon (GC-blue color), uncatalyzed KB300 loaded GC (black color), catalyst loaded GC (red color) recorded at 10 mV/s scan rate under saturated oxygen in 0.1 M $LiPF_6$ in Acetonitrile. For catalyst loaded GC, CV recorded under dynamic Ar gas flow showed no appreciable current. This is shown with purple color. Magnified OER and ORR features of both uncatalyzed and catalyzed cells are presented on the right side of the figure.

The blue color CV in the inset of Figure 4a represents the CV of the catalysts precursor alone obtained from a cathode half-cell with a Li metal anode. The catalyst is formed in-situ in the Li-O_2 cell at the end of the charge to 4.6 V. The redox behavior of each transition metal during Li intercalation in cathodic scan from 4.6 V allowed us to identify the nature of the transition metals in the OER and ORR potential ranges. The first oxidation peak appearing at around 3.3 V is due to Mn^{3+} oxidation followed by $Ni^{2+/}Ni^{4+}$ oxidation at about 3.8 V and the small oxidation peak just below 4.5 V is ascribed to the oxidation of Co^{3+}. In the cathodic scan the peaks at around 4.3 V and 3.6 V are attributed to the reduction of Co^{4+} and Ni^{4+}, respectively. Finally, the peak around 3 V is due to Mn^{4+} reduction. Identifying which portion of the parent structure (Li_2MnO_3 or $LiMO_2$) is contributing to Mn^{4+} reduction peak is outside of the scope of this paper. The detailed redox behavior of the catalyst was reported in our previous publication focusing on this material precursor as a Li-ion battery cathode.[15] A CV scan for the catalyst-containing Li-O_2 cell under argon gas flow (shown in fuchsia color in Figure 4a) did not generate any redox peaks from the catalyst material due to its very low concentration, although the redox reactions of the catalysts are occurring. This suggests that the peaks appearing in the Li-O_2 cell CVs are originating from O_2 redox reactions. The CV data obtained from the argon-purged cell also suggested that the electrolyte employed in Li-O_2 cells, 1 M $LiPF_6$ in TEGDME, have stability up to 4.6 V. We believe that the valence state of each transition metal is tuned for catalyst by the Li intercalation and de-intercalation reactions that take place in the cycling voltage range of the Li-O_2 cell. Coming back to the first oxygen reduction in the Li-O_2 cell, the catalyzed cell exhibited a distinct peak at around 3 V which is attributed to the formation of LiO_2 from the one-electron reduction of O_2. This behavior is reminiscent of the ORR in electrolytes based on the high donor number solvent dimethyl sulfoxide.[3] This peak was absent in the uncatalyzed cell. This suggests that catalyst-stabilized the superoxide formed initially in the catalyzed cell. In other words the chemical disproportion of LiO_2 to Li_2O_2 was delayed as pointed out in the step 2 reaction in the introduction (vide supra). Furthermore, the OER of the two cells are markedly different. The catalyzed cell showed a clear oxidation shoulder starting as early as 3.1 V unlike the uncatalyzed cell which did not show any OER peak until 3.7 V. Since the lifetime of the generated LiO_2 is finite, we analyzed the first reduction peak at different scan sweep rates to approximate its time dependency. This behavior is shown in Figure 4b. As the scan rate is decreased, the peak intensity corresponding to LiO_2 decreases. At high scan rates, the peak becomes more intense in good agreement with our previous data on the stability of LiO_2.[14] We also calculated the approximate time for the disproportion of LiO_2 to Li_2O_2. If one calculate the elapsed time between the onset of ORR (i.e. 3.1 V) and the end of the superoxide peak in Figure 4b, the lifespan of superoxide can be approximated. For instance, the time spent from the onset of the ORR potential (~3.1 V) and the end of superoxide peak (~2.8 V) at 25 μV/s was 3 hour and 20 minutes. Similarly, at the 100 μV/s scan rate this time was 1 hour 6 minutes. Based on these calculations, we can infer that the disproportionation of superoxide to peroxide is delayed at least 1 hour 6 minutes. This stabilized superoxide has remarkably higher lifetime in the catalyzed cell than that of uncatalyzed cell. In fact, there was no detectible superoxide peak at all in the uncatalyzed cell as can be seen in Figure 4a. Using SERS (Surface-enhanced Raman spectroscopy) Peng et al. found that LiO_2 decomposes to peroxide in less than 8 minutes on a gold electrode.[9] Here for the catalyzed cell we have found that superoxide can be stabilized for at least 1 hour without disproportion. This implies that the activation energy for O_2 reduction is decreased by our catalyst. Based on cyclic voltammograms and galvonastatic cycling test results discussed below, we calculated the capacity contribution from stabilized LiO_2 to be around 6%. That is, during discharge the capacity at about 2.7 V attributed to LiO_2 is around 1.1 mAh for the catalyzed cell which translates to a capacity of 115 mAh/g out of a total 1857 mAh/g capacity for an electrode weighing 10 mg. In this electrode 10 wt% is the actual catalyst, 80

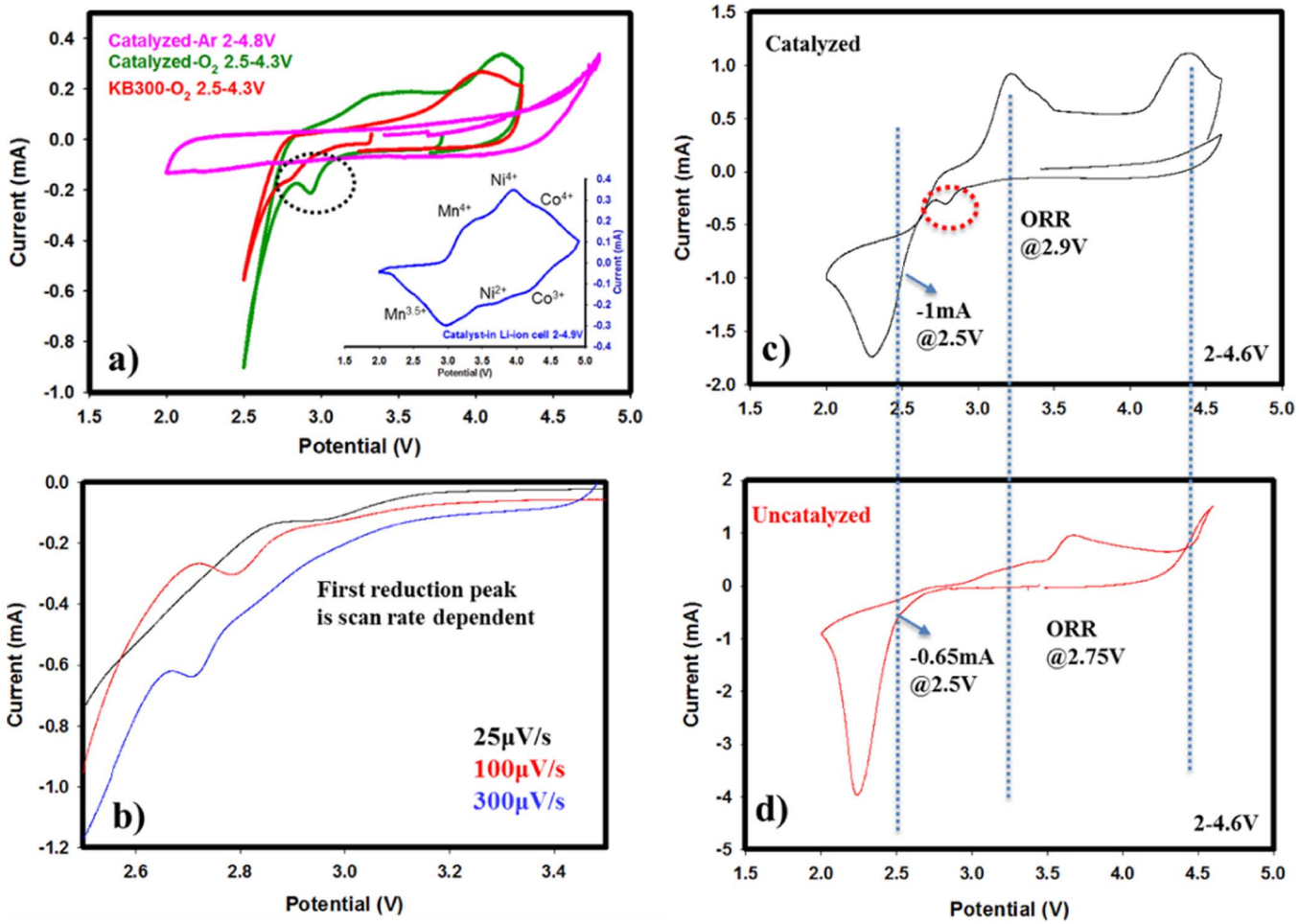

Figure 4. a-) Cyclic Voltammograms of Li-O_2 cells utilizing KB300 cathode, catalyzed cathode at a 100 μV/s scan rate between 2.5 and 4.3 V. Fuchsia color exhibits no OER and ORR behavior under Argon gas flow suggesting no impurities exist in the catalyst. Li-rich metal oxide containing Li-ion coin cell data was provided in the inset to show the redox behavior of each transition metal. b-) Scan rate dependency of the reduction peak appears below 3 V for catalyzed cell. CV data acquired at 100 μV/s between 2–4.6 V range for c-) catalyzed cell and d-) for uncatalyzed cell.

wt% is KB300 and 10 wt% is the binder PVDF. Similar loading of the KB300 electrode without catalyst delivered around 0.2 mAh at the same discharge potential. So the catalyzed capacity due to LiO_2 was 0.9 mAh, or 1.35 mg LiO_2 accumulated based on the theoretical LiO_2 capacity of 688 mAh/g. In other words, we obtained 1.35 mg of LiO_2 for 1 mg of catalyst during the first discharge. Figure 4c and 4d displays the CV behavior of the catalyzed and uncatalyzed cells, respectively, at a wider electrochemical window (2–4.6 V). As can be inferred from Figure 4c and 4d, the reduction current at 2.5 V is higher for the catalyzed cell due to reduced activation energy for ORR. This is also supported by the superoxide formation peak appearing at around 3 V. In contrast, the reduction current at 2 V is lower for the catalyzed cell compared to uncatalyzed cell. This further proves that during ORR at 2.5 V the reduction product, i.e. LiO_2 complexed with catalyst, passivated the surface thereby diminishing the intensity of 2 V reduction peak. The peak at 2 V during ORR is partially due to the reduction of LiO_2 to Li_2O_2. During OER, there is a sharp peak at 3.2 V for the catalyzed cell which is absent for the uncatalyzed cell. This peak pertains to the oxidation of LiO_2 also suggests stabilization of the LiO_2 intermediate by the catalyst. Overall, the discharge products of the catalyzed cell have a different oxidation reaction pathway. At the very least, it is clear from Figure 4c is that some of the reduction products are being oxidized at lower potentials in the catalyzed cell.

In a parallel experiment, we have examined the effect of activation of Li_2MnO_3. We were particularly interested in seeing whether the tuning of the Mn valence state in this segment of the composite catalyst structure affects either the ORR or OER processes. We ran CV studies at two different sweep direction of the catalyzed Li-O_2 cell. One of the cells was first charged up to 4.6 V followed by a discharge down to 2 V. The other cell was first discharged to 2 V without activating the Li_2MnO_3 region of the catalyst and then the Li-O_2 cell was charged to 4.6 V. Each cell was cycled twice and presented in Figure 5. It is clear from Figures 5a and 5b that a peak at around 3 V in the first discharge is visible in both. This we attribute to enhanced O_2 adsorption and formation of catalyst-stabilized LiO_2. Subsequently, the Li_2O_2 formation peak appears at about 2.5 V. Surprisingly, the OER process was quite different from each other. The catalyzed cell that was first discharged, displayed in Figure 5a, did not show a significant OER peak at around 3.2 V in the first charge whereas the same catalyzed cell if charged first to 4.6 V, shown in Figure 5b, exhibited a noticeable OER peak at around 3.2 V. This suggests that the activation of Li_2MnO_3 segment of the catalyst affects the OER response of catalyzed cells. This can be discerned further by looking at the second cycle of the cell that was discharged first (Figure 5a). In the second charging profile, after the activation of Li_2MnO_3 takes place in the first cycle, the OER response was quite similar to the cell that was charged first.

Galvanostatic cycling data.—Figure 6a–6d displays charge-discharge curves for both catalyzed and uncatalyzed Li-O_2 cells during cycling. It is apparent from the figures that the catalyzed cell has less voltage fade as well as the capacity fade. At the end of 13th discharge,

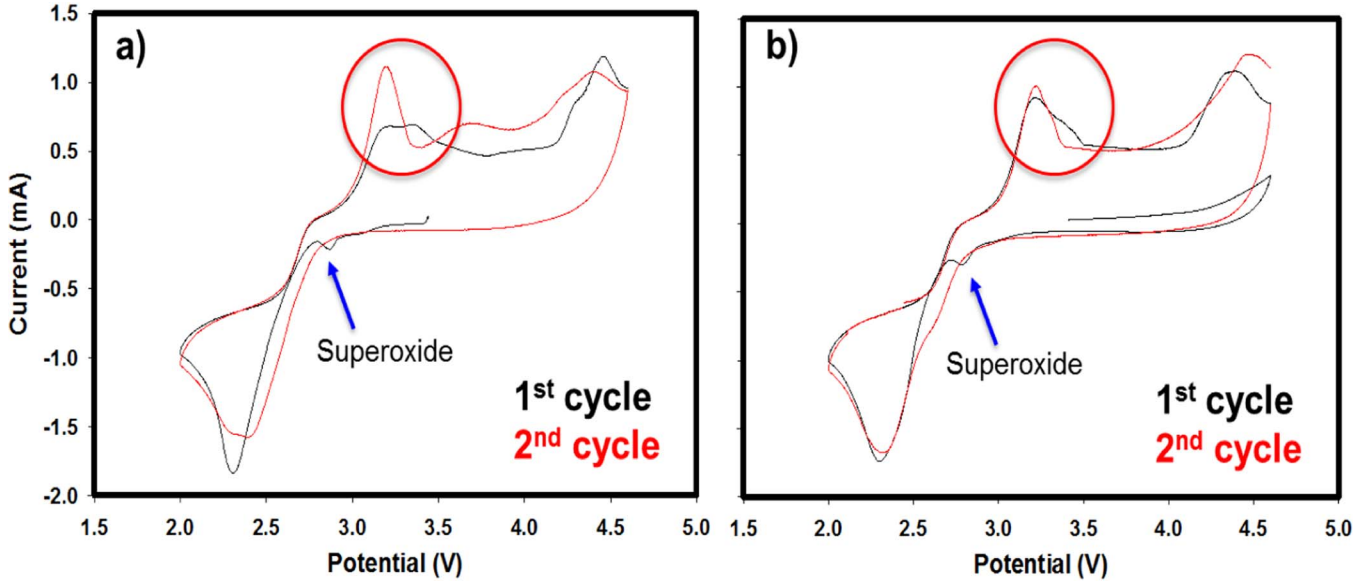

Figure 5. Cyclic Voltammograms of full Li-O_2 cells utilizing catalyzed KB300 cathode at a 100 μV/s scan rate between 2 and 4.6 V a-) first discharge to 2 V followed by a charge to 4.6 V b-) first charged to 4.6 V then discharged to 2 V.

the catalyzed cell could still deliver a capacity of 400 mAh/g above 2.5 V (Figure 6b), whereas uncatalyzed cell encountered significant voltage and capacity fades. During the charging process, i.e. OER, the catalyzed cell exhibited significantly more capacity under 4 V compared to the uncatalyzed cell. These data displayed in Figure 6c and 6d to demonstrate the bifunctionality of the catalyst reported in this paper. Voltage differences obtained from charge-discharge profiles at different cycles are shown in each figure.

We also compared the first full discharge-charge voltage profiles of the catalyzed and uncatalyzed cells. This is shown in Figure 7a where potential limits for discharge and charge processes were expanded to 2 V and 4.6 V, respectively. In order to verify that the capacity

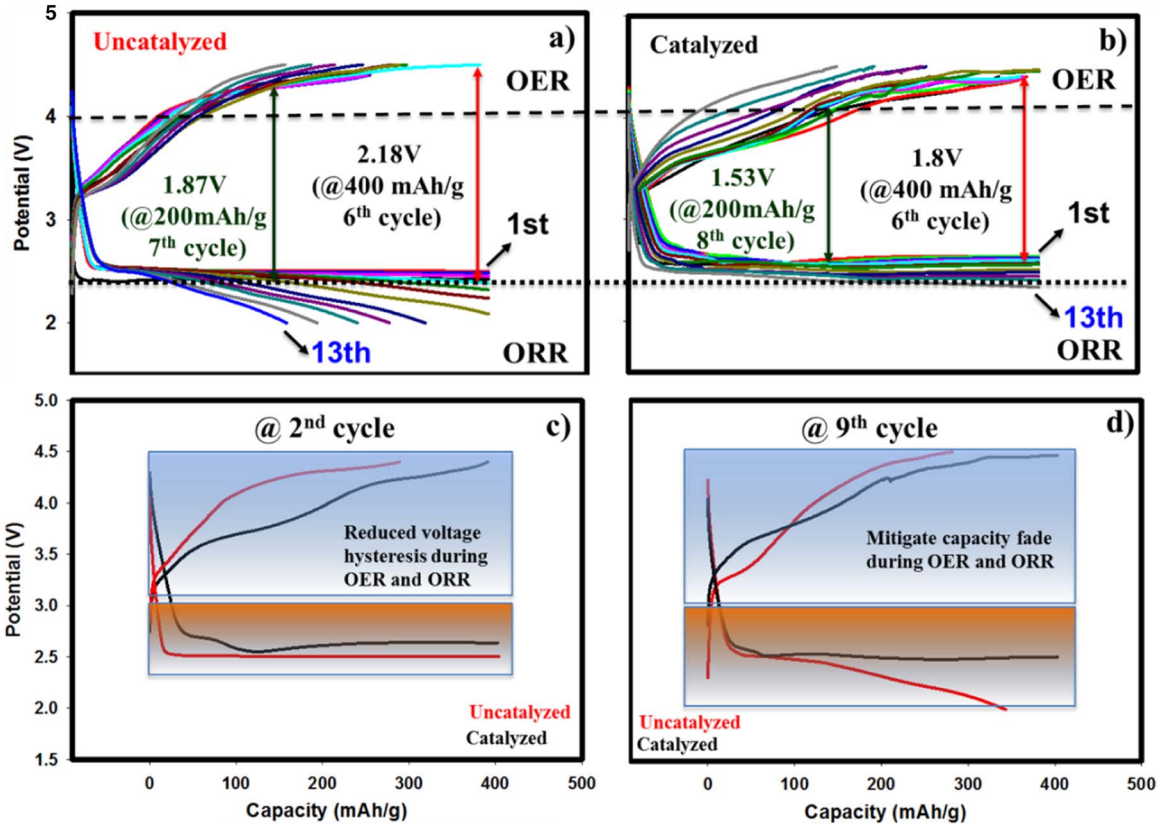

Figure 6. Galvanostatic charge-discharge profiles at 400 mAh/g depth of discharge with 0.1 mA/cm^2 current rate in 1 M $LiPF_6$ in TEGDME solvent under constant oxygen flow for a-) uncatalyzed cell b-) catalyzed cell. A clearer voltage profile comparison between uncatalyzed and catalyzed cells for c-) 2nd cycle and d-) 9th cycle.

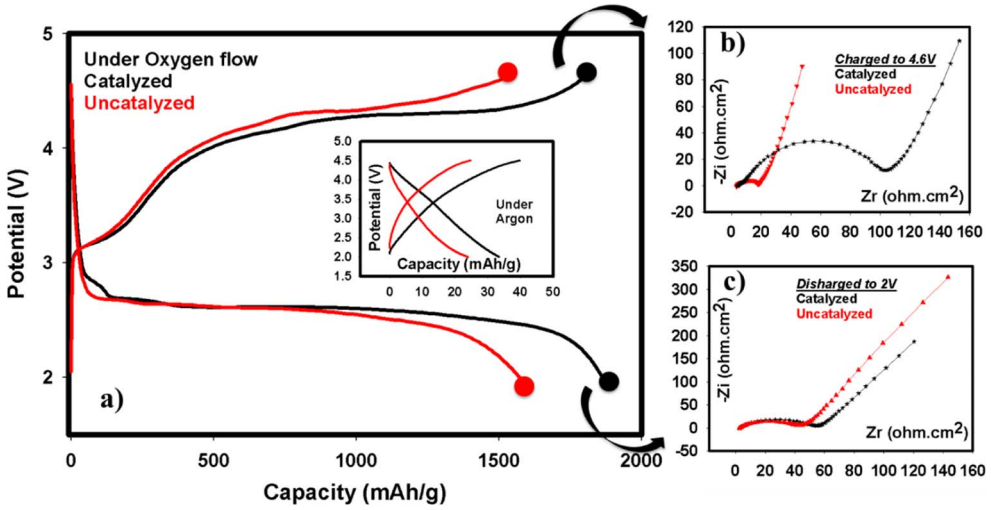

Figure 7. a-) 1st charge and discharge profiles for catalyzed and uncatalyzed cells at 0.1 mA/cm^2 applied current rate in 1 M $LiPF_6$ in TEGDME solvent under constant oxygen flow between 2–4.6 voltage limits. Inset figure shows the galvanostatic cycling data for both catalyzed and uncatalyzed cells with 0.1 mA/cm^2 current rate under Argon gas indicating no significant capacity was obtained via possible intercalation mechanism of Li ions to/from Li-rich metal oxide cathode. Impedance data are shown as Nyquist plots for catalyzed and uncatalyzed cells b-) after charged to 4.6 V and c-) after discharged to 2 V.

contribution from the intercalation of Li ions was negligible, we have performed the cycling protocol for the same cells under Ar gas flow. This is shown in the inset of Figure 7a and it clearly shows that no significant capacity is obtained from Li intercalation relative to the overall Li-O_2 cell discharge capacity.

Furthermore, the EIS data, displayed in Figure 7c, show that the catalyzed cell possess higher cell impedance at the end of discharge which is expected due to higher capacity leading to more insulating Li_2O_2 layers on the electrode. However, during charging the impedance of the catalyzed cell did not decrease as opposed to the uncatalyzed cell. At the end of charging, one would surmise that the effective OER catalyst decreases the resistance of the Li-O_2 cell due to the catalyzed oxidation of the discharge products. However in our case, the impedance of the catalyzed cell did not decrease after the charge. In contrast, the impedance of the catalyzed cell increased as can be seen in Figure 7b. The same experiments was repeated several times we obtained the identical results. Therefore, we came to the conclusion that the increased resistance of the catalyzed cell at the end of charging process is due to the irreversible and insulating product of Li_2O removal from Li_2MnO_3 structure which increase the overall resistance of the electrode. However, this electrochemical activation is an important step to create oxygen vacancies yielding favorable sites in the metal oxide catalysts for OER and ORR.

Post-test analysis of Li-O_2 cells.—Discharge products deposited in the electrodes were carefully examined using FESEM, XRD and Raman spectroscopy. Figure 8 displays several XRD patterns. The same figure also shows FESEM images of the electrodes corresponding to before and after discharge showing the accumulation of the discharge product on the surface of carbon cloth. Before cycling, the catalyzed cathode shows two major XRD peaks (approximately at 37 and 45 2θ-degrees) and a doublet peak at 65 2θ-degree associated with Li-rich layered-layered metal oxide pattern displayed earlier in Figure 2a. These peaks allowed us to determine whether the catalyst remain intact or not during cycling. After the first discharge, catalyzed and uncatalyzed cells revealed similar XRD patterns with lines at 33, 35 and 59 2θ-degree which correspond to Li_2O_2.[5] The only difference was that catalyzed cell (black color) showed a peak around 45 2θ-degree which is associated with the strong peak for the Li-rich layered metal oxide catalyst. The same peak was present even after 14 cycles (purple color) suggesting that catalyst was stable in the carbon electrode matrix and remains insoluble during cycling. These results also confirm that the discharge product is mainly Li_2O_2 for both catalyzed and uncatalyzed cells. Additionally, we attempted to identify LiO_2 species on the surface of the carbon electrode cloth by means of both XRD and Raman spectral data. XRD instrument is not able to identify superoxide formation, unless HE-XRD (high energy-XRD)

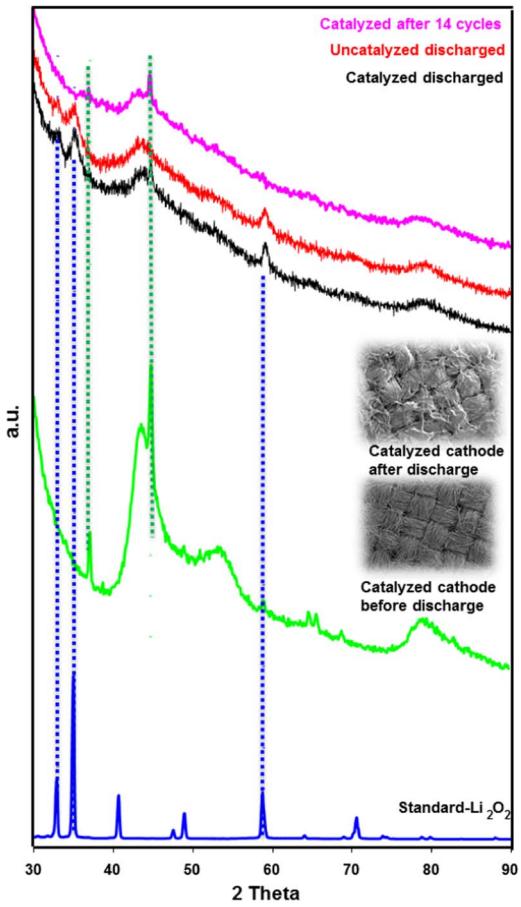

Figure 8. X-ray diffraction patterns of both catalyzed (black) and uncatalyzed (red) cells at their discharged states along with Li_2O_2 standard (blue). Yellow color of XRD pattern shows the pristine catalyzed cathode where strong peaks are indicative of Li-rich metal oxide patterns. Purple color displays the XRD patterns of catalyzed cell after 14 cycles at charged state proving that catalyst is intact with carbon cloth and insoluble in the electrolyte.

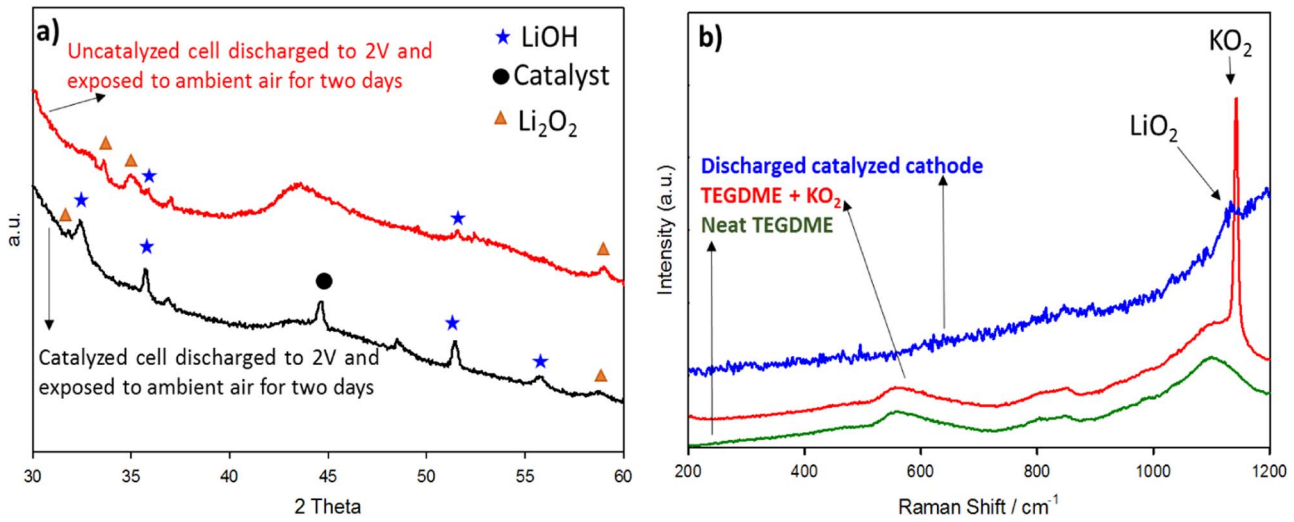

Figure 9. a-) X-ray diffraction patterns of both catalyzed (black) and uncatalyzed (red) cells at their discharged states. Both cells were exposed to atmospheric air for two days before the XRD measurements. b-) Ex-situ Raman spectrums collected immediately for the catalyzed cell at the discharge state along with neat TEGDME and TEGDME + KO_2 reference compounds.

is employed, as the conversion of lithium superoxide to lithium hydroxide have fast kinetics. Because of this, we exposed both catalyzed and uncatalyzed cells' carbon electrodes to ambient air for two days followed by XRD measurement. The idea of designing such an experiment is to verify whether the ingredients on the carbon cloths contain any lithium superoxide besides lithium peroxide. Figure 9a shows the XRD patterns of both catalyzed and uncatalyzed cathodes obtained after exposure to ambient air for two days. From this figure one can conclude that after the exposure to air for two days, the catalyzed cell produced sharper LiOH peaks at around 33, 36 and 52 2θ-degree than that generated in the carbon cathode from uncatalyzed cell. As explained above, this is an indication of the higher amount of superoxide present in the catalyzed cell electrode through catalyst-LiO_2 stabilization.

To further validate the stabilization of Li superoxide in catalyzed cells, we performed Raman experiments. For this, the discharged cathode with catalyst was removed from the Li-O_2 cell and placed in between two glass slides. The edges of the slides were covered with kapton tape in order to prevent air penetration into the sample. The spectra obtained from this experiment seen in Figure 9b clearly shows that there is a small peak appearing at the same location as the strong peak from the KO_2 reference sample. We were also curios whether the nucleation of the final discharge product Li_2O_2 differ when the catalyst was present in the cathode. For this we used FESEM for unraveling the morphological differences. Figure 10a–10b and 10c–10d show the discharge products for catalyzed and uncatalyzed cells at different magnifications. As can be seen in Figure 10c and 10d at different magnifications, the Li_2O_2 crystals in the uncatalyzed cell are needle-like. In the catalyzed cell as seen from the Figures 10a and 10b Li_2O_2 is formed through different nucleation mechanisms since the discharge product has a flower-like morphology. The latter morphology is believed to be facilitated by the slower decomposition of the catalyst-stabilized LiO_2. Therefore, we conclude that although the overall discharge products are the same for catalyzed and uncatalyzed cells, their nucleation processes are markedly different.

Proposed mechanistic details for enhanced OER and ORR of the catalyzed cell.—In order to understand the mechanistic details of the OER and ORR processes in the catalyzed cells, we used XAS for determining the valence states of each transition metal (TM) in the catalyst. Since the valence state of each TM is affected by the amount of Li extracted and/or inserted, approximating the d orbital filling is crucial to understand ORR and OER mechanisms during the course of Li-O_2 cell cycling. The significance of d orbital filling stems from the fact that they influence the bond strength between the adsorbate (here O_2) and transition metal in the catalyst. The energy level of s and p orbitals are preserved during the adsorption process.[25] Here, we take advantage of having multiple transition metals with different valence states present in the catalyst thereby TM-oxygen bond is appropriately triggered and tuned at different voltage regions. TM-Oxygen bond strength should not be too strong or too weak in order for the catalyst to adsorb and liberate O_2 during ORR and OER, respectively. Having mentioned these parameters, in an octahedral environment the electrons in d orbitals split into two sub-orbitals. These are known as high energy doublet (e_g) and low energy triplet (t_{2g}) in which electrons in e_g orbitals are more prone to react with the O_2 in the Li-O_2 cell than those of located in t_{2g}.[26] This is due to the fact that the e_g orbital set is more covalent than the t_{2g} orbitals.[27] The usage of e_g orbital for OER and ORR activity descriptor is very well recognized in aqueous media[26,28–31] and recently received a lot of attention in non-aqueous media as well.[12,32]

In this work, we have acquired near edge X-ray absorption (XANES) profiles of the absorbing atoms and their pre-edge regions

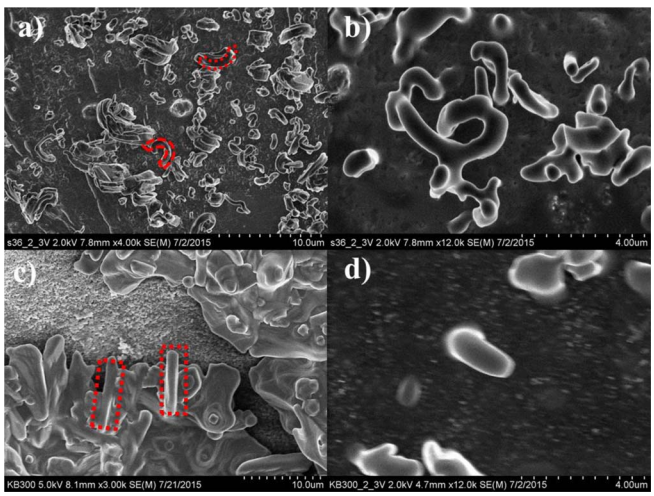

Figure 10. FESEM images after the 1st discharge at high and low magnifications for a,b-) catalyzed cell and c,d-) uncatalyzed cell advocating different nucleation (growth) mechanism. At higher magnifications due to charging effects (Li_2O_2 is not conductive enough) the quality of the pictures were diminished.

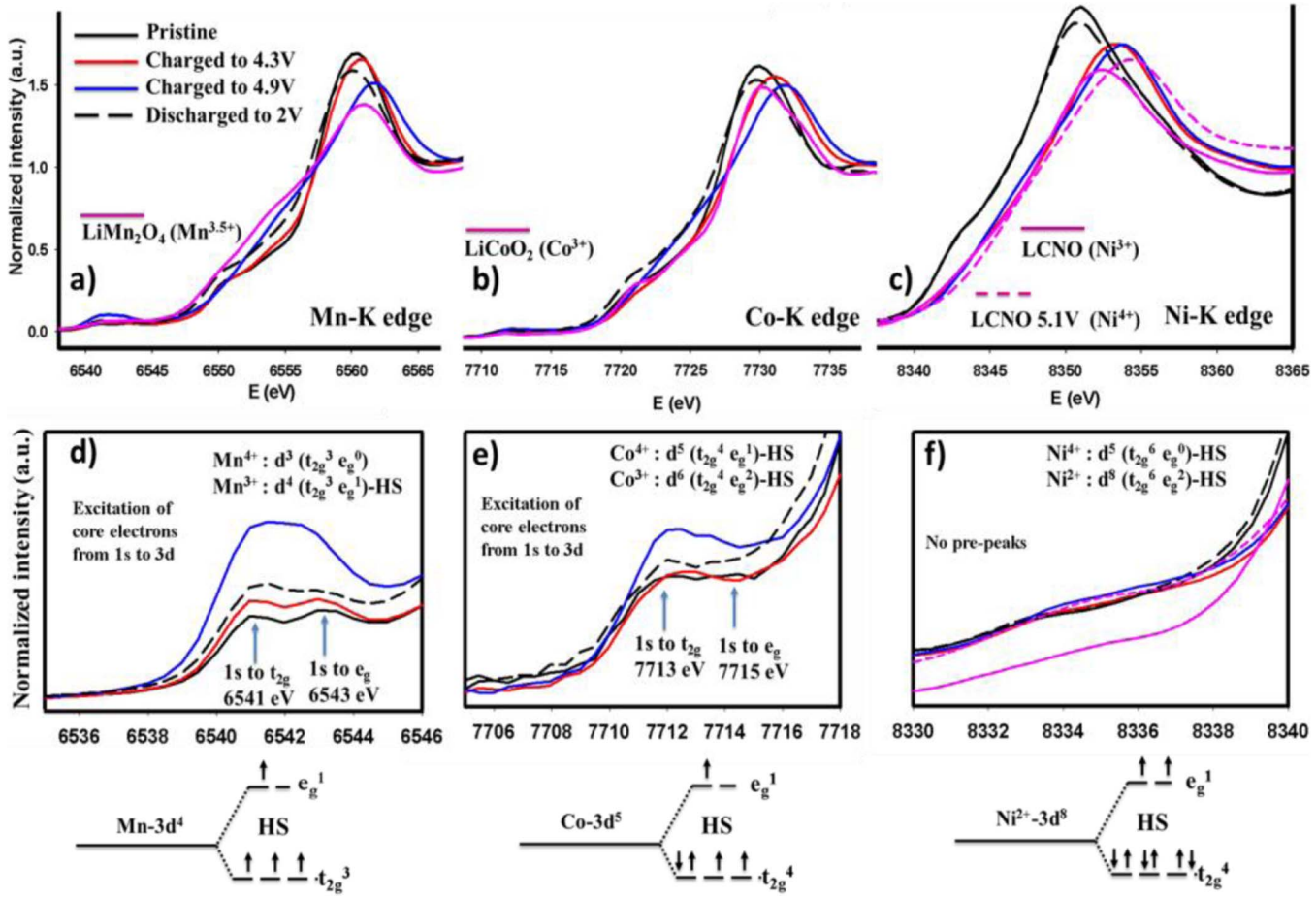

Figure 11. Near edge X-ray absorption (XANES) spectrums for a-) Mn, b-) Co, and c-) Ni K edges at different charge and discharge states along with reference compounds. The pre-edge regions were magnified and plotted in d, e and f for Mn, Co and Ni K edges, respectively. Under each figure, their d orbital filling in octahedral crystal field were schematized.

in K edges to identify the d electron configuration. The shape and threshold energy position of a XANES profile can provide critical information of ligand interaction and oxidation states of absorbing atom. Figure 11 displays the XANES spectrums of three transition metal present in the catalyst. Each XANES figure and its respective pre-edge regions were magnified and shown underneath figure along with the schematized d orbital fillings. For a transition metal with noncentrosymmetric environment in octahedral system, the pre-edge region is usually caused by 1s →3d transition. These regions have either a singlet or a doublet peak depending on the nature of d orbital filling. The latter is caused by the 1s → t_{2g} and 1s → e_g transitions within the 1s → 3d transition and can be assigned to track the changes during the cycling in each sub-orbitals i.e. t_{2g} and e_g. Figure 11a, 11b and 11c show the XANES profiles of the TMs at different potentials during cycling. Although we did not charge the Li-O_2 cell to 4.9 V, we intended to show the redox behavior of TMs in such extremely high overpotentials. From Figure 11a, we concluded that Mn can be oxidized to little more than $Mn^{3.5+}$ at 4.9 V based on the spinel reference material. At these high overpotentials, the e_g sub-orbital, as can be seen in Figure 11d, was empty and therefore we can rule out the catalytic activity of Mn. However at 4.3 V the average oxidation state of Mn is around 3.5^+ identical to spinel reference. We expect some catalytic activity at this potential during OER, however still the filling fraction of e_g sub-orbital is not close to unity. In contrast, during the discharge process at 2 V, the valence state of Mn atoms were less than 3.5^+, close to 3^+. At this low discharge potentials the e_g orbital filling was close to unity suggesting that Mn was catalytically active during ORR. This can easily be understood from the Figure 11d where the two pre-edge peaks were formed causing e_g orbital filling approximately to 1. Figure 11b depicts the X-ray absorption feature of Co metal where Co is being oxidized to more than 3^+ at 4.3 V during the charging process. Although at 4.9 V Co atoms were further oxidized, it was reported[33] that Co atoms were completely oxidized to 4^+ at 4.4 V. Based on the pre-edge features, including e_g sub-orbital filling fraction, shown in Figure 11e, at high potentials Co appears to be catalytically active for OER process. During the discharge the valence state of Co decreased to 3^+ where e_g sub-orbitals were filled with two electrons yielding inactive catalytic sites for ORR. Figure 11c displays the valence state variation of Ni absorbing atom where it is evidenced that Ni is oxidized to 4^+ at 4.3 V. Neither at 2 V nor at 4.3 V Ni appears to have catalytically active sites based on both very low pre-edge intensities as well as e_g orbital filling fraction shown in Figure 11f. However, having a Ni atom in the structure seems to balance the electronic charge of Mn and Co atoms which determine the overall electro-catalytic activity of the Li-rich metal oxide.

Based on the above discussion, in Scheme 1 we propose the reactions in catalyzed and uncatalyzed cells during ORR and OER processes.

Both catalyzed and uncatalyzed cells yield Li_2O_2 as the final discharge product. The only difference in the catalyzed cell is that the initially formed LiO_2 is stabilized by the Mn atom present in the catalyst. The catalyst-stabilized LiO_2 in the carbon matrix is further reduced to lithium peroxide probably also with the aid of the Mn atom present in the catalyst. Because the intermediate product is stabilized through Mn atoms located in Li-rich metal oxide and its decomposition to Li_2O_2 occurs at a slower rate, the product is morphologically different

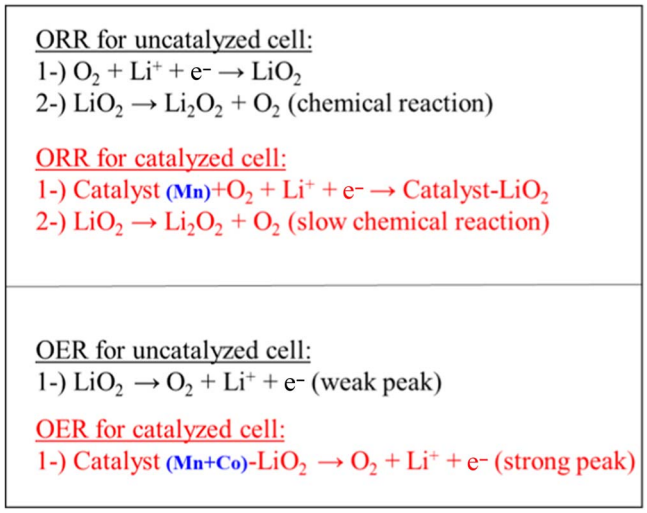

Scheme 1. The schematic of OER and ORR processes of catalyzed and uncatalyzed Li-O_2 cells.

from that in the uncatalyzed cell. During the OER process, the discharge product in the catalyzed cell is oxidized through a different step from that in the uncatalyzed cell. The sharp peak occurring at around 3.1 V in the CV during oxidation is the evolution of O_2 from the catalyst-stabilized lithium superoxide. This is achieved mainly via catalytically active e_g orbitals of Co. The partially filled e_g orbitals of Mn atoms could be having an effect on OER as well which needs further confirmation.

Conclusions

In this work, we demonstrated the ability to use a Li-rich layered-layered metal oxide as a bifunctional catalyst for Li-air battery applications. We found each transition metal has its own characteristic ability to produce catalytically active sites during the course of cycling. By tuning the valence state simultaneously during the ORR and OER processes, the catalyst yielded highly active centers toward ORR and OER. Ex-situ XRD and Raman results revealed that the uncatalyzed cells have Li_2O_2 as the final product during discharge, whereas for the catalyzed cell the discharge product comprised of both Li_2O_2 and LiO_2. FESEM investigations suggested that the nucleation mechanism of the discharge products were markedly different. The XAS data unveiled the critical information of sub-orbital fillings, i.e. e_g and t_{2g}, of each transition metal. We have established that Mn plays an important role during ORR and Co was the major contributor to the OER process along with the contribution from Mn. The Li-rich metal oxide layered-layered oxides can provide oxygen deficient sites that could enhance the catalytic activity if one charges it to high potentials in the first cycle. We believe that next-generation cathode materials based on Li-rich layered-layered metal oxides from Li-ion batteries have great potential to be recycled at the end of their life by simply employing them as an ORR/OER catalyst for metal-air batteries, thereby alleviating environmental concerns.

Acknowledgment

Financial support from US Army Cerdec via subcontract No: GTS-S-15-015 is gratefully acknowledged.

References

1. K. M. Abraham and Z. Jiang, *Journal of The Electrochemical Society*, **143**, 1 (1996).
2. K. M. Abraham, *ECS Transactions*, **3**, 67 (2008).
3. C. O. Laoire, S. Mukerjee, K. M. Abraham, E. J. Plichta, and M. A. Hendrickson, *The Journal of Physical Chemistry C*, **114**, 9178 (2010).
4. C. O. Laoire, S. Mukerjee, K. M. Abraham, E. J. Plichta, and M. A. Hendrickson, *The Journal of Physical Chemistry C*, **113**, 20127 (2009).
5. C. Laoire, S. Mukerjee, E. J. Plichta, M. A. Hendrickson, and K. M. Abraham, *Journal of The Electrochemical Society*, **158**, A302 (2011).
6. C. J. Allen, J. Hwang, R. Kautz, S. Mukerjee, E. J. Plichta, M. A. Hendrickson, and K. M. Abraham, *The Journal of Physical Chemistry C*, **116**, 20755 (2012).
7. S. A. Freunberger, Y. Chen, N. E. Drewett, L. J. Hardwick, F. Bardé, and P. G. Bruce, *Angewandte Chemie International Edition*, **50**, 8609 (2011).
8. S. A. Freunberger, Y. Chen, Z. Peng, J. M. Griffin, L. J. Hardwick, F. Bardé, P. Novák, and P. G. Bruce, *Journal of the American Chemical Society*, **133**, 8040 (2011).
9. Z. Peng, S. A. Freunberger, L. J. Hardwick, Y. Chen, V. Giordani, F. Bardé, P. Novák, D. Graham, J.-M. Tarascon, and P. G. Bruce, *Angewandte Chemie International Edition*, **50**, 6351 (2011).
10. B. D. Adams, C. Radtke, R. Black, M. L. Trudeau, K. Zaghib, and L. F. Nazar, *Energy & Environmental Science*, **6**, 1772 (2013).
11. H.-G. Jung, Y. S. Jeong, J.-B. Park, Y.-K. Sun, B. Scrosati, and Y. J. Lee, *ACS Nano*, **7**, 3532 (2013).
12. K. P. C. Yao, Y.-C. Lu, C. V. Amanchukwu, D. G. Kwabi, M. Risch, J. Zhou, A. Grimaud, P. T. Hammond, F. Barde, and Y. Shao-Horn, *Physical Chemistry Chemical Physics*, **16**, 2297 (2014).
13. S. H. Oh and L. F. Nazar, *Advanced Energy Materials*, **2**, 903 (2012).
14. M. J. Trahan, Q. Jia, S. Mukerjee, E. J. Plichta, M. A. Hendrickson, and K. M. Abraham, *Journal of The Electrochemical Society*, **160**, A1577 (2013).
15. M. N. Ates, S. Mukerjee, and K. M. Abraham, *RSC Advances*, **5**, 27375 (2015).
16. S. H. Oh, R. Black, E. Pomerantseva, J.-H. Lee, and L. F. Nazar, *Nat Chem*, **4**, 1004 (2012).
17. F. Cheng, T. Zhang, Y. Zhang, J. Du, X. Han, and J. Chen, *Angewandte Chemie International Edition*, **52**, 2474 (2013).
18. T. Y. Ma, Y. Zheng, S. Dai, M. Jaroniec, and S. Z. Qiao, *Journal of Materials Chemistry A*, **2**, 8676 (2014).
19. C. S. Johnson, J. S. Kim, C. Lefief, N. Li, J. T. Vaughey, and M. M. Thackeray, *Electrochemistry Communications*, **6**, 1085 (2004).
20. M. N. Ates, Q. Jia, A. Shah, A. Busnaina, S. Mukerjee, and K. M. Abraham, *Journal of The Electrochemical Society*, **161**, A290 (2014).
21. M. N. Ates, S. Mukerjee, and K. M. Abraham, *Journal of The Electrochemical Society*, **161**, A355 (2014).
22. M. N. Ates, S. Mukerjee, and K. M. Abraham, *Journal of The Electrochemical Society*, **162**, A1236 (2015).
23. R. E. Ruther, A. F. Callender, H. Zhou, S. K. Martha, and J. Nanda, *Journal of The Electrochemical Society*, **162**, A98 (2015).
24. Q. Wu, V. A. Maroni, D. J. Gosztola, D. J. Miller, D. W. Dees, and W. Lu, *Journal of The Electrochemical Society*, **162**, A1255 (2015).
25. W. T. Hong, M. Risch, K. A. Stoerzinger, A. Grimaud, J. Suntivich, and Y. Shao-Horn, *Energy & Environmental Science*, **8**, 1404 (2015).
26. Y. Matsumoto, H. Yoneyama, and H. Tamura, *Journal of Electroanalytical Chemistry and Interfacial Electrochemistry*, **83**, 237 (1977).
27. T. E. Westre, P. Kennepohl, J. G. DeWitt, B. Hedman, K. O. Hodgson, and E. I. Solomon, *Journal of the American Chemical Society*, **119**, 6297 (1997).
28. F. Calle-Vallejo, N. G. Inoglu, H.-Y. Su, J. I. Martinez, I. C. Man, M. T. M. Koper, J. R. Kitchin, and J. Rossmeisl, *Chemical Science*, **4**, 1245 (2013).
29. A. Grimaud, K. J. May, C. E. Carlton, Y.-L. Lee, M. Risch, W. T. Hong, J. Zhou, and Y. Shao-Horn, *Nat Commun*, **4** (2013).
30. J. Suntivich, K. J. May, H. A. Gasteiger, J. B. Goodenough, and Y. Shao-Horn, *Science*, **334**, 1383 (2011).
31. J. Park, H. Kim, K. Jin, B. J. Lee, Y.-S. Park, H. Kim, I. Park, K. D. Yang, H.-Y. Jeong, J. Kim, K. T. Hong, H. W. Jang, K. Kang, and K. T. Nam, *Journal of the American Chemical Society*, **136**, 4201 (2014).
32. J. Suntivich, H. A. Gasteiger, N. Yabuuchi, H. Nakanishi, J. B. Goodenough, and Y. Shao-Horn, *Nat Chem*, **3**, 546 (2011).
33. X. Yu, Y. Lyu, L. Gu, H. Wu, S.-M. Bak, Y. Zhou, K. Amine, S. N. Ehrlich, H. Li, K.-W. Nam, and X.-Q. Yang, *Advanced Energy Materials*, **4**, n/a (2014).